



## Full length article

## On the origin of a remarkable increase in the strength and stability of an Al rich Al-Ni eutectic alloy by Zr addition

Prafull Pandey<sup>a,\*\*\*</sup>, Surendra Kumar Makineni<sup>a,b,\*\*</sup>, Baptiste Gault<sup>b</sup>, Kamanio Chattopadhyay<sup>a,\*</sup>

<sup>a</sup> Department of Materials Engineering, Indian Institute of Science, Bangalore, 560012, Karnataka, India

<sup>b</sup> Max-Planck-Institut für Eisenforschung GmbH, 40237, Düsseldorf, Germany

## ARTICLE INFO

## Article history:

Received 20 December 2018

Received in revised form

19 March 2019

Accepted 19 March 2019

Available online 24 March 2019

## Keywords:

Aluminium alloys

Precipitation hardening

High temperature

Mechanical properties

Atom probe tomography

Transmission electron microscopy

## ABSTRACT

The effect of Zr addition to Al rich binary  $\alpha$ -Al - Al<sub>3</sub>Ni eutectic cast alloy (Al-3.1 at.% Ni) in enhancing the microstructural stability and strength at high temperature is demonstrated. On subsequent heat treatment after casting, nanometric coherent L1<sub>2</sub> ordered Al<sub>3</sub>Zr precipitates form inside the  $\alpha$ -Al that strengthen the alloy. Additionally, remarkable stability of eutectic microstructure was observed even after 100 h of annealing at 400 °C. The synergetic effect of the strengthening of the  $\alpha$ -Al matrix by coherent Al<sub>3</sub>Zr precipitates and the low coarsening rate of the Al<sub>3</sub>Ni rods results in a significant increase in high temperature hardness and yield strength of the alloy. The tensile yield strength of the annealed Al-3.1Ni-0.15Zr alloy (400 °C, 10 h) tested at 250 °C is found to be 185 ± 10 MPa, which is 1.5 times higher than the corresponding binary Al-3.1Ni alloy. The experimentally determined average rod size (radius) during annealing at 400 °C follows the classical matrix diffusion controlled LSW-based coarsening model for both binary Al-3.1Ni and ternary Al-3.1Ni-0.15Zr alloys. The calculated coarsening rate constant values based on modified LSW coarsening model are 10.3 and 4.1 nm<sup>3</sup>/s for Al-3.1Ni and Al-3.1Ni-0.15Zr alloys, respectively. Atom probe tomographic (APT) investigations of the heat-treated ternary alloy unambiguously reveal segregation of Zr solute at the  $\alpha$ Al/Al<sub>3</sub>Ni interface in addition to the presence of the strengthening Al<sub>3</sub>Zr ordered precipitates in the  $\alpha$ -Al matrix. The segregation hinders the interdiffusion of Al and Ni in the eutectic and, thereby, increasing the stability of the eutectic phase at high temperature.

© 2019 Acta Materialia Inc. Published by Elsevier Ltd. All rights reserved.

## 1. Introduction

In the automotive market, aluminium and its alloys, due to their light weight, are mostly consumed (up to 70% of the total content of the automobiles) in the fabrication of components in a powertrain that includes engine, clutch, transmission and various drive shafts [1]. Cast Al alloys constitute the major fraction (~85–90%) that are primarily based on the Al-Si eutectic system [2]. Improving the mechanical strength and sustainability of aluminum alloys at higher temperatures is a major technological goal since a large

portion of engine parts, such as cylinder heads, valve filters are exposed to temperatures exceeding 200 °C and can be replaced with newer high strength alloys. This in turn, can lead to a higher engine operating temperature thereby enhancing efficiency. It is well known that the addition of Cu and Mg to Al-Si alloys strengthen the alloys by precipitation of coherent intermetallic phases [3–6]. However, the precipitates rapidly coarsen at temperatures greater than 200 °C resulting in a loss of alloy strength [7–9].

Recently,  $\alpha$ Al-Al<sub>3</sub>Ni eutectic alloy has shown promise as a replacement for Al-Si alloys [10–16]. This system has a higher eutectic temperature of ~640 °C (compared to 577 °C for Al-Si), comparable casting ability, hot tear resistance and better mechanical properties [15,17–20]. In the Al-Ni eutectic microstructure, the equilibrium Al<sub>3</sub>Ni phase (orthorhombic crystal structure, *Pnma*) appears as alternate rods in soft  $\alpha$ -Al matrix (face-centered-cubic, fcc, *Fm $\bar{3}$ m*). The eutectic derives its strength from the composite

\* Corresponding author.

\*\* Corresponding author. Max-Planck-Institut für Eisenforschung GmbH, 40237, Düsseldorf, Germany.

\*\*\* Corresponding author.

E-mail addresses: [prafull1011@gmail.com](mailto:prafull1011@gmail.com) (P. Pandey), [sk.makineni@mpie.de](mailto:sk.makineni@mpie.de) (S.K. Makineni), [kamanio@iisc.ac.in](mailto:kamanio@iisc.ac.in) (K. Chattopadhyay).

structure of hard Al<sub>3</sub>Ni rods grown in the soft  $\alpha$ -Al matrix during eutectic solidification [10,11,21]. However, the binary Al-Ni eutectic alloy shows a relatively low yield strength of ~150 MPa at room temperature, which is not suited for engineering applications [22]. Further, instabilities during annealing at high temperatures and rapid coarsening deteriorate the strength and restrict the high temperature application of Al-Al<sub>3</sub>Ni eutectic alloy [20,23–26]. Hence, the addition of solutes that facilitates the strengthening of  $\alpha$ -Al matrix by inducing high temperature stable coherent precipitates can improve both room and high temperature mechanical properties of this alloy system. Addition of transition metals (TM) like Sc, Zr and V, resulted in precipitation of strengthening coherent intermetallic phases of L1<sub>2</sub> ordered structure with the stoichiometry Al<sub>3</sub>TM in the  $\alpha$ -Al matrix [27–32]. These precipitates are relatively stable at high temperatures (~300 °C) [33–37]. However, due to their limited solid solubility in  $\alpha$ -Al, the volume fractions of the precipitated intermetallic phases are low. Combining the strengthening of the  $\alpha$ -Al matrix by coherent precipitates and strengthening through the eutectic composite can be promising and has been explored in recent time. It was shown that addition of Sc or Zr/V to Al-based eutectic cast alloys has resulted in an improvement in mechanical properties that is attributed mainly to the precipitation of coherent Al<sub>3</sub>Zr, Al<sub>3</sub>Sc or Al<sub>3</sub>(Zr,V) precipitates in  $\alpha$ -Al matrix [12,16,19,38,39]. In particular, the addition of Sc is shown recently to significantly improve the mechanical properties including creep properties of Al-Al<sub>3</sub>Ni eutectic alloy [39]. However, understanding the nature of contribution from these solutes towards the origin of high temperature strength in these alloys as well as the stability of the eutectic composites at high temperatures provide opportunities for further studies. In the present work, through a combined study of atom probe tomography (APT), transmission electron microscopy (TEM) and experiments on long term microstructural stability, the effect of Zr addition to the binary Al-3.1 at.% Ni eutectic alloy has been studied. Attempts have been made to rationalize the enhancement of the stability of microstructure of ternary alloy at elevated temperatures compared to its binary counterpart as well as the contribution of different strengthening processes towards the evolution of strength of these alloys.

## 2. Experimental details

### 2.1. Sample preparation and electron microscopy

Alloys of compositions Al-3.1 at.%Ni and Al-3.1 at.%Ni-0.15 at.%Zr were prepared by arc melting of mixtures of 99.99% pure constituent elements under an argon atmosphere at a vacuum level of ~10<sup>-5</sup> mbar. Alloys were arc melted 8 times to avoid segregation of elements, in particular, Zr. After melting, the alloys were chill cast using Cu molds to yield 3 mm diameter rods and 3 mm\*10 mm\*75 mm (thickness\*width\*length) slabs. The absence of microsegregation as well as the composition of the bulk alloy in the cast samples, were confirmed by elemental mapping using wavelength dispersive (WDS) spectrometer in an electron probe microanalyzer (JEOL, JXA-8530F) equipped with a field emission gun (FEG) operating at 15 kV with 50 nA current. The nominal and analyzed compositions of the prepared alloys along with their designation used in the present study are presented in Table 1.

Chill cast rods of both the alloys were cut into smaller pieces and annealed in a muffle furnace at 400 °C for different durations. Microstructural examination for the annealed alloys was carried out by using a scanning electron microscope (SEM) equipped with a FEG (FEI, SIRION XL-30). Prior to SEM imaging, all samples were chemically etched using Keller's reagent having a composition of 95 vol% distilled water-2.5 vol% HNO<sub>3</sub>-1.5 vol% HCl-1.0 vol% HF. A detailed characterization of the phases and precipitates present in the alloys were also carried out using a transmission electron microscope (TEM, FEI Tecnai, F-30) equipped with a FEG source and energy dispersive spectrometer (EDS). Samples for TEM investigation were prepared by cutting 3 mm disks from the as-cast and annealed rods and mechanically polished up to a thickness ~80  $\mu$ m. This was followed by argon ion-milling using a precision ion polishing system (PIPS, GATAN make) to finalize the electron transparent specimens.

### 2.2. Atom probe tomography (APT)

Atomic-scale compositional analysis was carried out using atom probe tomography. Site-specific specimens were fabricated using a dual beam SEM/focused-ion-beam (FIB) instrument (FEI Helios NanoLab 600i) in conjunction with an in-situ lift-out method [40]. In order to protect from the Ga ion damage during milling, first, a platinum (Pt) layer of ~200 nm thickness was deposited on the region-of-interest (ROI). A final cleaning procedure with 2 kV and 8 pA current was carried out to remove the surface damage occurred during preparation of the tip. APT measurements were carried out using a 'reflectron' equipped local electrode atom probe (LEAP, 5000 XR, Cameca Instruments) operated in the laser pulsing mode with a pulse repetition rate of 200 kHz and a pulse energy of 0.4 nJ. The specimen base temperature was kept at 60 K with a set detection target rate of 5 ions at every 1000 pulses. The data reconstruction and analysis were performed using the software package IVAS™ 3.8.2.

### 2.3. Evaluation of mechanical properties

The preliminary heat treatment response of the alloys was confirmed by measuring the Vickers hardness using a microhardness tester (Future Tech, FM-800) at 100 gm load with 10 s dwell time. Screw-driven uniaxial testing machine (Zwick/Roell) was used to conduct the tensile tests. Tensile tests were carried out at room temperature (25 °C) and at 250 °C at a strain rate of 10<sup>-3</sup> s<sup>-1</sup>. For high temperature tests at 250 °C, the samples were pre-heated for 15 min so that homogenous temperature is achieved in the specimen and the testing system. The micro-tensile specimens were prepared in the shape of flat dog-bone with dimensions of 2 mm width, 0.5 mm thickness, 8 mm gauge length and radius of curvature of 2 mm.

### 2.4. Stereographical measurements

For the measurement of spacing between the Al<sub>3</sub>Ni rods of the as-cast alloys, a line perpendicular to the rods were drawn and the grey contrast values vs distance were plotted by using the ImageJ software. The peak in grey value is taken as the center of the rod

**Table 1**

Alloy's nominal compositions and measured compositions (in atomic %) using WDS in EPMA with its designation are listed.

Alloy Designation	Nominal Composition (at.%)	Measured Composition (at.%)
Al-3.1Ni	Al-3.10 at.%Ni	Al-3.20 ± 0.15 at.%Ni
Al-3.1Ni-0.15Zr	Al-3.10 at.%Ni-0.15 at.%Zr	Al-3.25 ± 0.12 at.%Ni-0.16 ± 0.03 at.%Zr

and the distance between the two adjacent maxima in grey values is taken as the rod spacing. On the other hand, for the spacing measurements from the annealed samples, we selected regions which contain rods along longitudinal directions as well as cross sections of rods having rounded shape  $Al_3Ni$  phase. The distance (spacing) in both the cases were measured using ImageJ software program. At least 50 such measurements were taken and finally, average value is reported.

For the rod size calculation, we first measured the cross-sectional area ( $A$ ) of each rod using ImageJ software program. The obtained value of  $A$  for each rod was then used to calculate a circular areal-equivalent radius ( $R_{eq}$ ) by using the following equation

$$A = \pi * R_{eq}^2 \quad (1)$$

where,  $A$  is the calculated cross-sectional area of a rod and  $R_{eq}$  is the circular areal-equivalent radius of the rod. 500 such rods were chosen from 4 to 5 different eutectic colonies and finally averaged to calculate the average circular areal-equivalent radius,  $\langle R_{eq} \rangle$ . The error in the measurement of the  $\langle R_{eq} \rangle$  was calculated using the following relation

$$\sigma_R = \frac{\sigma_{std}}{\sqrt{N}} \quad (2)$$

where,  $\sigma_R$  is the error in the  $\langle R_{eq} \rangle$  measurement,  $\sigma_{std}$  is the

standard deviation of the  $\langle R_{eq} \rangle$ , and  $N$  is the number of rods used for the measurements.

### 3. Results

#### 3.1. As-cast microstructure of Al-3.1Ni alloy and the influence of Zr addition

At the Al-rich end of the Al-Ni phase diagram (see [Supplementary Fig. S1](#)), a eutectic reaction comprising  $L \rightarrow \alpha-Al + Al_3Ni$  occurs at a composition of Al-2.7 at.% Ni at 639.9 °C [41]. [Fig. 1\(a\)](#) shows a secondary electron (SE) image of the binary as-cast Al-3.1Ni alloy. It exhibits a eutectic microstructure containing in-situ grown rods of bright contrast embedded within the grey phase. The eutectic colonies demarcated by the green dotted lines have an average spacing of 13  $\mu m$ . [Fig. 1\(b\)](#) shows the SE image for 0.15 at.% Zr added Al-3.1Ni-0.15Zr alloy. The eutectic composition of the alloy was shifted to hypoeutectic side with the microstructure containing similar eutectic phases (region between green dotted line) and primary dendrites of  $\alpha-Al$  (in-between eutectic colonies), as marked in [Fig. 1\(b\)](#). The WDS elemental mapping, [Supplementary Fig. S2](#), shows a uniform distribution of Zr in the eutectic colonies without any segregation or another phase formation. In the Al-3.1Ni alloy, the identification of the two phases was carried out by diffraction analysis in TEM. [Fig. 1\(c\)](#) shows the

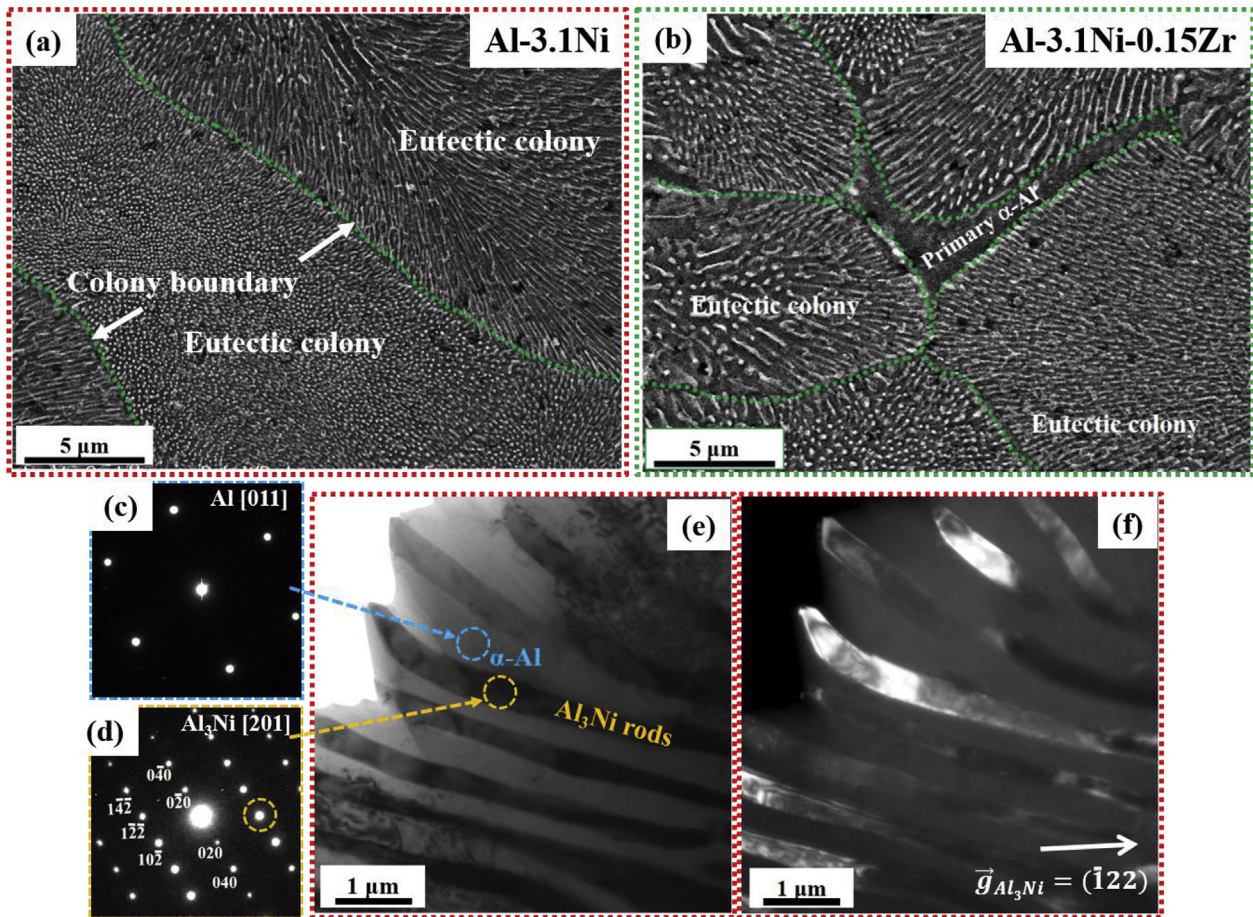


**Fig. 1.** Secondary electron (SE) images of the as-cast (a) Al-3.1Ni and (b) Al-3.1Ni-0.15Zr alloys showing a eutectic microstructure containing bright contrast rods ( $Al_3Ni$  phase) and grey matrix ( $\alpha-Al$  phase). Al-3.1Ni-0.15Zr alloy shows a presence of primary  $\alpha-Al$  dendrites between eutectic colonies (region between green dotted lines). (c) SAED pattern along [011] direction from the grey matrix of the as-cast Al-3.1Ni alloy. (d) SAED pattern along [201] direction from the bright rod phase of the as-cast Al-3.1Ni alloy. (e) bright-field and (f) dark-field images taken using T22 reflection of  $Al_3Ni$  phase along [201] zone axis showing eutectic rods are embedded in  $\alpha-Al$  matrix. (For interpretation of the references to color in this figure legend, the reader is referred to the Web version of this article.)

selected area electron diffraction (SAED) pattern taken from the grey phase. The pattern can be indexed as [011] zone axis pattern for fcc  $\alpha$ -Al (space group:  $Fm\bar{3}m$ ). Similarly, Fig. 1(d) shows the SAED pattern from the rod that is indexed as the [201] zone axis pattern corresponding to the  $Al_3Ni$  intermetallic phase with an orthorhombic crystal structure (space group:  $Pnma$ ). Fig. 1(e) and (f) show bright-field and dark-field images of eutectic rods embedded in  $\alpha$ -Al matrix taken using the  $\bar{1}22$  reflection of  $Al_3Ni$  phase along the [201] zone axis.

Zr addition significantly influences the  $Al_3Ni$  rods spacing, as shown in Supplementary Fig. S3. The rods spacing increases from  $370 \pm 60$  nm in the Al-3.1Ni alloy to  $500 \pm 100$  nm for the Al-3.1Ni-0.15Zr alloy under identical solidification conditions. Additionally, in as-cast condition, Al-3.1Ni alloy shows a hardness value of  $70 \pm 4$  HV which, within the standard error, is comparable to the hardness value of  $64 \pm 3$  for Al-3.1Ni-0.15Zr alloy.

### 3.2. Microstructural evolution of Al-3.1Ni and Al-3.1Ni-0.15Zr alloys during annealing at 400 °C

Vickers micro-hardness (HV) was used to evaluate the microstructural stability for both the alloys after annealing at 400 °C. Fig. 2(a) shows a plot of the variation of HV vs annealing time at 400 °C for both the alloys. The HV for Al-3.1Ni alloy decreases monotonically from 76 (1 h) to 59 after 100 h of annealing while for Al-3.1Ni-0.15Zr alloy, HV increases from 79 (1 h) to 92 after 10 h and reduces to 85 after 100 h of annealing. In comparison, the HV of Al-3.1Ni-0.15Zr alloy is 1.5 times greater than the Al-3.1Ni alloy after 100 h of annealing. These differences are further elucidated by carrying out the microstructural examination of both the alloys after different annealing times.

The temporal evolution of eutectic phases ( $\alpha$ -Al and  $Al_3Ni$ ) in Al-3.1Ni and Al-3.1Ni-0.15Zr alloys after annealing at 400 °C is illustrated as back-scattered SEM micrographs in Fig. 2(b–e) and supplementary Figs. S4 (a–f). The Al-3.1Ni alloy after 10 h exhibits morphological instabilities and spheroidization of  $Al_3Ni$  rods

(Fig. 2(b)). After 100 h of annealing, the rods further coarsen (Fig. 2(c)). In contrast, any sign of instabilities or morphological changes of  $Al_3Ni$  rods in Al-3.1Ni-0.15Zr alloy is not evident even after 100 h of annealing, as shown in Fig. 2(e). Fig. 2(f) shows the change in  $Al_3Ni$  rods spacing with annealing time for both the alloys. The frequency plots of rod spacing distribution during annealing at 400 °C for both the alloys are shown in Supplementary Fig. S5. In Al-3.1Ni alloy, the average value of spacing increases from  $500 \pm 90$  nm after 10 h to  $700 \pm 120$  nm after 100 h. In contrast, a slower coarsening kinetics of  $Al_3Ni$  rods were observed for Al-3.1Ni-0.15Zr alloy with an average spacing increasing from  $470 \pm 70$  nm after 10 h to  $580 \pm 80$  nm after 100 h of annealing at 400 °C.

To know the cause of this significant enhancement in the microstructural stability of Al-3.1Ni-0.15Zr alloy at 400 °C, TEM investigations were carried out on annealed samples. Fig. 3(a) shows a high-angle-annular-darkfield (HAADF) scanning TEM image from a eutectic region for Al-3.1Ni-0.15Zr alloy after 10 h of annealing at 400 °C. A clear Z-contrast image of  $Al_3Ni$  rods in  $\alpha$ -Al matrix could be observed. Additionally, the contrast variation in the  $\alpha$ -Al (see inset of Fig. 3(a)), evidences the presence of nanometric precipitates distributed uniformly in the matrix. Fig. 3(b) shows SAED patterns from the  $\alpha$ -Al region taken along the [001] and [011] zone axes that show the presence of additional superlattice reflections along with the fundamental fcc  $\alpha$ -Al reflections. These superlattice reflections correspond to the fcc-based  $L1_2$  ordering similar to that exhibited by  $Ni_3Al$  phase in Ni-based superalloys [42]. The dark-field micrograph, shown in Fig. 3(c), taken from the 010 superlattice spot along [001] direction illuminates the coherently embedded spherical nanometric precipitates with size < 10 nm, consistent with that seen in HAADF image of Fig. 3(a). The coherent nature of the precipitates can be seen by a high resolution electron micrograph from the region containing a precipitate along [001] fcc  $\alpha$ -Al zone axis, as shown in Fig. 3(d). The fast Fourier transform (FFT) patterns from the surrounding  $\alpha$ -Al matrix and the ordered precipitate shows a cube-on-cube orientation relationship. Hence, the strengthening of the Al-3.1Ni-0.15Zr alloy

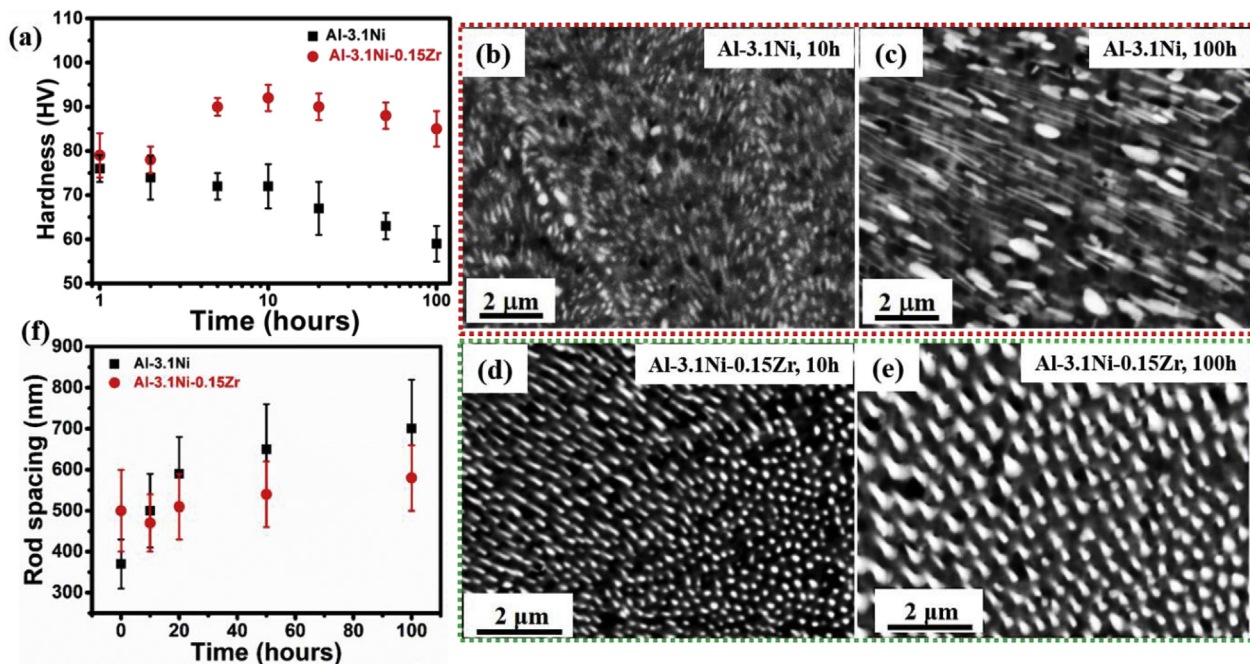
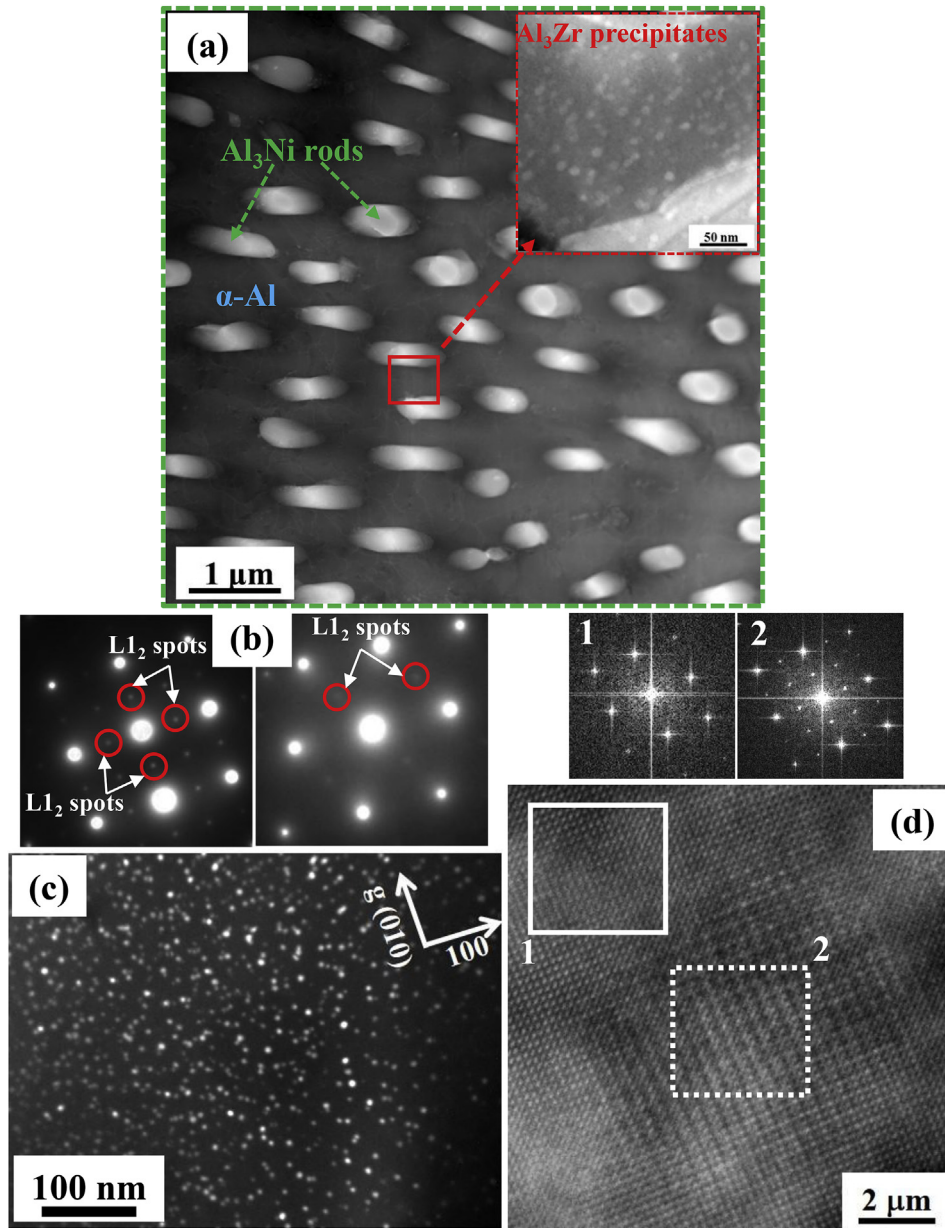


Fig. 2. (a) Evolution of Vickers micro-hardness number (HV) for the Al-3.1Ni and Al-3.1Ni-0.15Zr alloys during isothermal annealing at 400 °C from 1 h to 100 h. SEM micrographs in back-scattered electron (BSE) mode showing microstructural evolution during isothermal annealing at 400 °C: (b) Al-3.1Ni; (d) Al-3.1Ni-0.15Zr alloys for 10 h and (c) Al-3.1Ni; (e) Al-3.1Ni-0.15Zr alloys for 100 h. (f) Temporal evolution of average rod spacing for the Al-3.1Ni and Al-3.1Ni-0.15Zr alloys during isothermal annealing at 400 °C.



**Fig. 3.** (a) HAADF-STEM image of the heat-treated Al-3.1Ni-0.15Zr alloy (annealed at 400 °C for 10 h) showing Z contrast image of bright Al<sub>3</sub>Ni rods in α-Al matrix. The inset of Fig. (a) reveals the presence of precipitates distributed uniformly in the matrix. (b) The SAED patterns along the [001] and [011] directions of α-Al matrix of the heat-treated Al-3.1Ni-0.15Zr alloy showing superlattice reflections corresponding to L<sub>12</sub> ordering. (c) Centered dark-field TEM image from a superlattice diffraction spot showing uniformly distributed precipitates in the α-Al matrix. (d) High resolution image taken from [001] oriented grain showing coherency between L<sub>12</sub> ordered spherical precipitate and α-Al matrix. The fast Fourier transform (FFT) patterns from the matrix and precipitate confirm cube-on-cube orientation relationship between them.

is expected to be associated with the formation of these coherent spherical precipitates in the α-Al matrix.

Compositional analysis for these spherical precipitates in Al-3.1Ni-0.15Zr alloy annealed for 10 h was carried out using APT. Fig. 4(a) shows the APT reconstruction of a specimen prepared from the α-Al phase region containing a distribution of Al atoms (yellow color) and iso-composition interface (red color) with a threshold value of 16 at.% Zr. These interfaces, which are Zr enriched, highlight the regions that correspond to the strengthening spherical precipitates. A plot of composition profiles, Fig. 4(b), across one of the precipitates, show the precipitate composition to be ~21.9 at.% Zr, close to the stoichiometry Al<sub>3</sub>Zr with a solubility of Ni ~ 3.2 at.% in the precipitate.

APT investigations were also carried out for 100 h annealed

sample of Al-3.1Ni-0.15Zr alloy to understand the influence of Zr addition on the stability of eutectic microstructure at 400 °C. Fig. 5(a) shows a HAADF-STEM image of an APT specimen containing bright regions corresponding to Al<sub>3</sub>Ni rod and grey α-Al matrix. Fig. 5(b) shows the APT reconstruction of the specimen with the distribution of Al atoms (yellow color) and iso-composition interfaces with a threshold value of 16 at.% Zr (red color) depicting the presence of spherical Al<sub>3</sub>Zr precipitates in the α-Al matrix. In addition, it also contains a Ni-rich (green color) region corresponding to part of an Al<sub>3</sub>Ni rod delineated by an iso-composition interface with a threshold value of 19 at.% Ni (green color). Fig. 5(c) shows the composition profiles across one of the spherical precipitates confirming the Al<sub>3</sub>Zr stoichiometry, similar to the precipitate composition obtained in the 10 h annealed specimen.

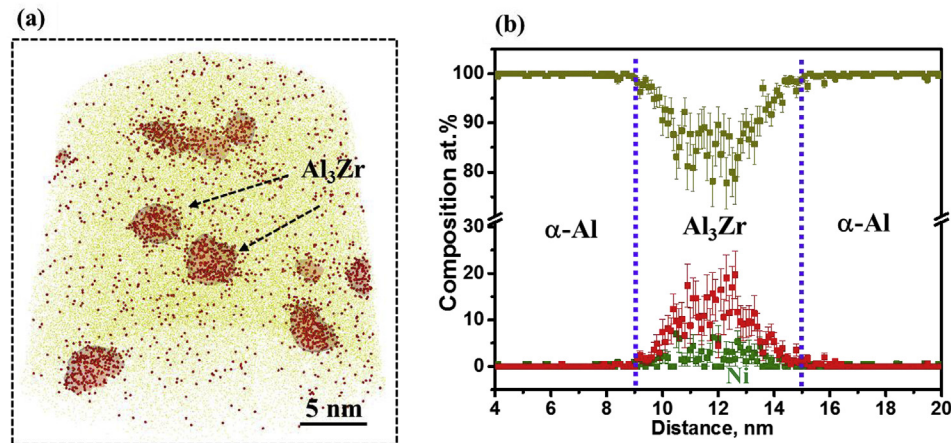


**Fig. 4.** (a) An APT reconstruction of the Al-3.1Ni-0.15Zr alloy subjected to annealing at 400 °C for 10 h, showing Zr rich (red color) spherical precipitates (delineated by 16 at.% Zr) distributed in the  $\alpha$ -Al (yellow color) matrix (b) The composition profiles across a precipitate showing these precipitates to be Zr rich and close to  $\text{Al}_3\text{Zr}$  stoichiometry. (For interpretation of the references to color in this figure legend, the reader is referred to the Web version of this article.)

The composition profiles across the Ni-rich region and  $\alpha$ -Al show that the rod phase composition is close to the stoichiometry of  $\text{Al}_3\text{Ni}$  intermetallic (Fig. 5(d)). Fig. 5(e) shows a magnified view (black dotted rectangle in (d)) of the composition profiles across the  $\alpha$ -Al/ $\text{Al}_3\text{Ni}$  interface. A significant enrichment Zr  $\sim 0.16$  at.% was observed at the interface relative to either  $\alpha$ -Al or  $\text{Al}_3\text{Ni}$  phase. The Zr enrichment at the  $\alpha$ -Al/ $\text{Al}_3\text{Ni}$  interface is consistent and also confirmed by APT analysis of another specimen containing the interface whose analysis is shown in Supplementary Fig. S6, however, with a value of  $\sim 0.34$  at.%.

### 3.3. Mechanical properties

To evaluate the 0.2% proof stress (PS), uniaxial tensile tests were performed at room temperature (25 °C) and 250 °C. The engineering stress-strain plots obtained from the tensile tests are shown in Fig. 6(a). The properties are summarized in Table 2. The effect of precipitation strengthened  $\alpha$ -Al matrix can be seen through an improvement in the room temperature tensile properties of 10 h annealed Al-3.1Ni-0.15Zr alloy compared to the as-cast Al-3.1Ni alloy. The 0.2% PS values for Al-3.1Ni and Al-3.1Ni-0.15Zr alloys are found to be  $200 \pm 9$  MPa and  $255 \pm 13$  MPa, respectively. The room temperature ultimate tensile stress (UTS) value increases from  $308 \pm 14$  MPa for Al-3.1Ni alloy to  $350 \pm 11$  MPa for annealed Al-3.1Ni-0.15Zr alloy, whereas no significant difference in the ductility (elongation %, El%) is observed. At 250 °C, the UTS for Al-3.1Ni alloy significantly decreases to  $132 \pm 6$  MPa, while the annealed Al-3.1Ni-0.15Zr alloy still exhibits a UTS of  $218 \pm 8$  MPa. The comparison of 0.2% PS values for the two alloys is presented as a bar chart in Fig. 6(b). The improved tensile properties of Al-3.1Ni-0.15Zr alloy at elevated temperatures reflect relatively superior microstructural stability compared to Al-3.1Ni alloy. Furthermore, the room temperature 0.2% PS of the Al-3.1Ni and Al-3.1Ni-0.15Zr alloys subjected to isothermal annealing at 400 °C for 100 h is observed to be 155 and 245 MPa (see Fig. 6(b)), respectively. This increment in strength by more than 1.5 times further provides testimony to the microstructural stability of Al-3.1Ni-0.15Zr alloy.

## 4. Discussion

### 4.1. Influence of Zr addition on as-cast microstructure of Al-3.1Ni alloy

The comparison of as-cast microstructures for Al-3.1Ni and Al-

3.1Ni-0.15Zr alloy shows the difference in the  $\alpha$ -Al/ $\text{Al}_3\text{Ni}$  eutectic spacing. The phenomenon of increase in eutectic spacing with ternary addition was reported earlier by Liu et al. [43]. The increase in spacing is attributed to a decrease in the solidification velocity due to the requirement of the third element (Zr) to diffuse away ahead of the solidification front since Zr atoms do not partition to  $\text{Al}_3\text{Ni}$ . This leads to an enhanced time for the coupled lateral diffusion of Al and Ni atoms leading to a coarser microstructure. The eutectic colony size (cell spacing) for the ternary Al-3.1Ni-0.15Zr alloy is calculated to be 18  $\mu\text{m}$ .

### 4.2. Strength contribution from eutectic fraction in heat-treated Al-3.1Ni-0.15Zr alloy

The mechanical properties of a eutectic alloy critically depend on the length scale of the microstructure. Recently an experimental correlation of yield properties with eutectic colony size has been reported [44,45]. Several successful attempts have also been made to correlate the length scale of microstructure with strength by using the Hall-Petch type relationship between yield strength ( $\sigma_{YS}$ ) and eutectic spacing ( $\lambda$ ) by the equation [46,47].

$$\sigma_{YS} = \sigma_0 + K \times \left(\lambda^{-\frac{1}{2}}\right) \quad (3)$$

Where,  $\sigma_{YS}$  is the yield strength contribution from the eutectic,  $\sigma_0$  is the frictional stress of the matrix,  $K$  is a constant and  $\lambda$  is the eutectic spacing (rod spacing). To obtain the values of  $K$  and  $\sigma_0$ , we first measured the yield strength values for Al-3.1Ni alloy containing eutectic microstructure with varying spacing obtained by an isothermal annealing at 400 °C for different durations. Fig. S7 (see supplementary information) shows the plot between the measured  $\sigma_{YS}$  and  $\lambda^{-\frac{1}{2}}$ . A linear regression analysis of the data gives a slope ( $K$ ) of 3065 (MPa. $\sqrt{\text{nm}}$ ) and the intercept ( $\sigma_0$ ) value of 41.5 (MPa). These values were assumed to be constant and used to evaluate the eutectic strength contribution in Al-3.1Ni-0.15Zr alloy. The calculated contribution from eutectic ( $\sigma_{eutectic}$ ) by using the above equation (3) for the ternary alloy after 10 h and 100 h of annealing at 400 °C are  $\sim 183$  MPa and 168 MPa, respectively.

### 4.3. Strength contribution from coherent $\text{Al}_3\text{Zr}$ precipitates in annealed Al-3.1Ni-0.15Zr alloy

Depending on the precipitate size, the strengthening contribution comes from two mutually competing mechanisms [48]. The

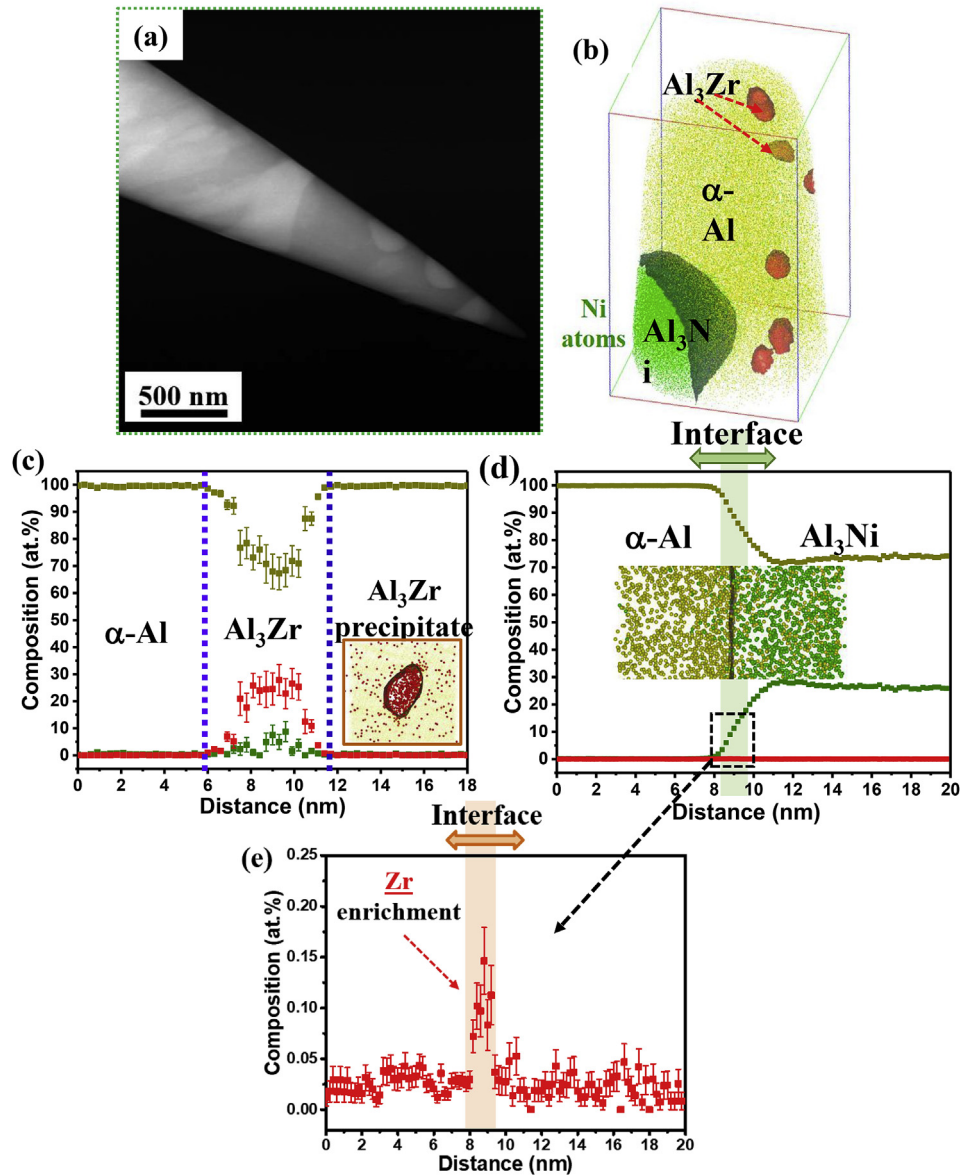


**Fig. 5.** (a) HAADF-STEM image of an APT specimen for Al-3.1Ni-0.15Zr alloy subjected to isothermal annealing at 400 °C for 100 h showing bright Al<sub>3</sub>Ni rods in the grey  $\alpha$ -Al matrix. (b) APT reconstruction of the specimen showing several Zr rich (red color) spherical precipitates and a Ni rich (green color) region. (c) The composition profiles across the  $\alpha$ -Al/Zr rich precipitate interface showing very low solubility of Ni in the Al<sub>3</sub>Zr precipitates. The inset shows cross-section of one of the spherical Al<sub>3</sub>Zr precipitates. (d) The composition profiles across the interface between  $\alpha$ -Al and Ni rich region revealing Ni rich region to be of the stoichiometry of Al<sub>3</sub>Ni with negligible solubility of Zr. (e) The composition profile of Zr (red color) across the  $\alpha$ -Al/Al<sub>3</sub>Ni interface shows interfacial segregation of Zr. (For interpretation of the references to color in this figure legend, the reader is referred to the Web version of this article.)

first of the mechanisms involves shearing of the precipitates by mobile dislocations, which operates for relatively smaller precipitate size. In contrast, the second mechanism involves bowing of dislocations around the precipitates, which operates for comparatively bigger precipitate size. When the shearing mechanism operates, there are three factors that contribute to the yield strength and they are: (i) order strengthening ( $\Delta\sigma_{order}$ ); (ii) coherency strengthening ( $\Delta\sigma_{coherency}$ ) and (iii) modulus strengthening ( $\Delta\sigma_{modulus}$ ). Appendix A gives the associated equations for the respective mechanisms.

Fig. 7(a) shows the plots between the strength increments from these mechanisms as a function of precipitate radius by keeping the respective measured stereological values of Al<sub>3</sub>Zr precipitates present in the annealed Al-3.1Ni-0.15Zr alloy, as shown in Table 4. From the plots, we see that there are two critical radii of

precipitates, marked as red and green arrows, indicating a transition of mechanisms operational on the application of load. The first corresponds to  $r_{c1}$  with a value of 2.5 nm and another  $r_{c2}$  with a value of 3.2 nm. Below  $r_{c1}$ , the contribution to strengthening from ordering ( $\Delta\sigma_{order}$ ) is predominant, while above  $r_{c1}$ , coherency + modulus strengthening dominates ( $\Delta\sigma_{coherency} + \Delta\sigma_{modulus}$ ). Beyond  $r_{c2}$ , strengthening from Orowan looping mechanism prevails. A Brief explanation of these mechanisms are included in Appendix A and also can be found in basic metallurgical textbooks. The estimated  $r_{c2}$  value of 3.2 nm for the transition of strengthening mechanism from shearing to Orowan looping mechanism is close to the reported values for Al<sub>3</sub>Zr in Al-0.1Zr alloy (~2.8 nm) and higher than Al<sub>3</sub>Sc in Al-0.3Sc alloy (~2.2 nm) [49–52]. The predicted precipitate size is greater for Al<sub>3</sub>Zr than that for Al<sub>3</sub>Sc precipitates due to the lower lattice mismatch with the  $\alpha$ -

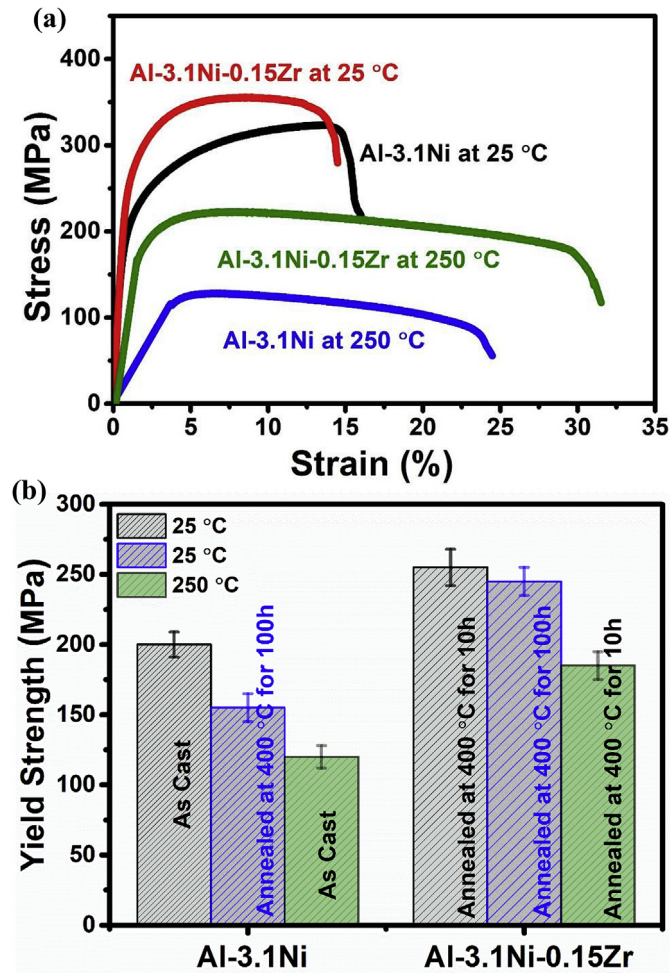


Fig. 6. (a) Tensile stress vs strain plots at temperatures of 25 °C and 250 °C for the as-cast Al-3.1Ni alloy and annealed Al-3.1Ni-0.15Zr alloy (after isothermal annealing at 400 °C for 10 h). (b) Bar plots comparing the 0.2% proof stress (yield strength) at 25 °C and 250 °C for the Al-3.1Ni and annealed Al-3.1Ni-0.15Zr alloys.

Al resulting in the increase of critical radius beyond which the coherency at the interface is lost.

In the present Al-3.1Ni-0.15Zr alloy, the spherical Al<sub>3</sub>Zr precipitates have an average size of  $2.5 \pm 1.0$  nm for 10 h and  $4.0 \pm 1.0$  nm for 100 h annealed samples at 400 °C. From the plots in the Fig. 7(a), the major contribution of strengthening in 10 h annealed alloy will be due to either order ( $\Delta\sigma_{order}$ ) or coherency + modulus ( $\Delta\sigma_{coherency} + \Delta\sigma_{modulus}$ ) mechanisms, whichever has a higher value. For 100 h annealed alloy, the major strengthening contribution is from Orowan looping mechanism due to the average precipitate size  $> r_{c2}$  (3.2 nm). We also like to convey that the Al<sub>3</sub>Zr precipitates have a certain size distribution with some of their sizes  $> r_{c2}$  for 10 h and  $< r_{c2}$  for 100 h in the annealed alloy. This might lead to an overlap of the type of

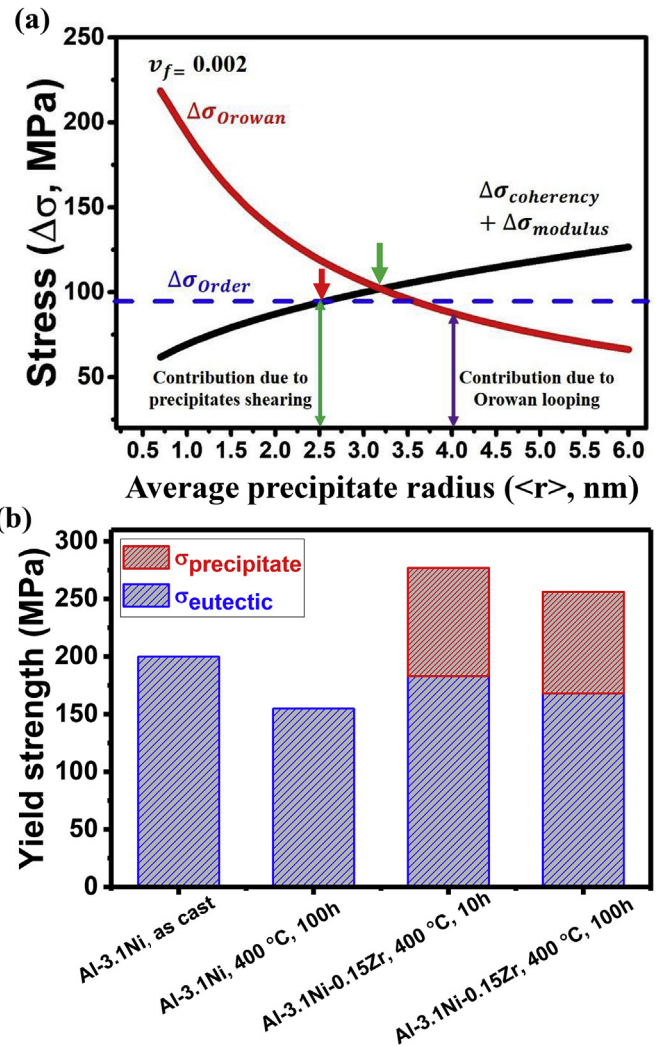


Fig. 7. (a) Variation in the different contributions to the strength from the ordered Al<sub>3</sub>Zr precipitates as a function of the average precipitate radius ( $\langle r \rangle$ ) for the Al-3.1Ni-0.15Zr alloy annealed at 400 °C. The curves represent estimated strengthening contributions due to ordering ( $\Delta\sigma_{order}$ ) as a dashed blue line, coherency and modulus as a solid black line ( $\Delta\sigma_{coherency} + \Delta\sigma_{modulus}$ ) and Orowan looping as solid red line ( $\Delta\sigma_{Orowan}$ ). The equilibrium precipitate volume fraction (400 °C for 10 h annealed condition) value of  $v_f = 0.002$  is used for the calculation. (b) The bar plot showing the different contribution to the room temperature (25 °C) yield strength for the as-cast and 100 h exposed at 400 °C Al-3.1Ni alloy, and Al-3.1Ni-0.15Zr alloy after annealing at 400 °C for 10 and 100 h. (For interpretation of the references to color in this figure legend, the reader is referred to the Web version of this article.)

mechanisms operating in the annealed alloys. However, we will assume that only the major contributions will be effective for the strengthening of the alloy. Table 3 shows the calculated strength increment values by using the equations in appendix A and experimental values in Table 4 for both the annealed alloys. In the sample annealed for 10 h, with an average Al<sub>3</sub>Zr precipitate size of

Table 2  
Experimentally determined yield strength (YS), ultimate tensile strength (UTS) and elongation (El%) for the as cast Al-3.1Ni and annealed Al-3.1Ni-0.15Zr alloys tested at room temperature (25 °C) and 250 °C.

Alloys	Temperature (°C)	YS (MPa)	UTS (MPa)	Elongation (%)
Al-3.1Ni	25 °C	200 ± 9	308 ± 14	~14
	250 °C	120 ± 8	132 ± 6	~20
Al-3.1Ni-0.15Zr, annealed at 400 °C for 10 h	25 °C	255 ± 13	350 ± 11	~12
	250 °C	185 ± 10	218 ± 8	~30

**Table 3**

Estimated strength from different contributions at room temperature for the Al-3.1Ni-0.15Zr alloy annealed at 400 °C for 10 and 100 h. Estimated strengths are also compared with the experimentally obtained strength.

Alloy and heat treatment condition	Average precipitate radius (<r>), nm	Strength increment due to Al <sub>3</sub> Zr precipitates (MPa)				Estimated yield strength (MPa)			Experimental yield strength (MPa)
		$\Delta\sigma_{order}$	$\Delta\sigma_{coherency} + \Delta\sigma_{modulus}$	$\Delta\sigma_{orowan}$	$\sigma_{eutectic}$	$\sigma_{precipitate}$	$\sigma_{total}$		
Al-3.1Ni-0.15Zr, annealed at 400 °C for 10 h	2.5	94	94	119	183	94	277	255 ± 13	
Al-3.1Ni-0.15Zr, annealed at 400 °C for 100 h	4.0	94	110	88	168	88	256	245 ± 10	

**Table 4**

Temporal evolution of the average precipitate radius (<r>), precipitate number density (N<sub>v</sub>) and volume fraction (v<sub>f</sub>) for the Al-3.1Ni-0.15Zr alloy annealed at 400 °C for 10 and 100 h.

Alloy and heat treatment condition	Precipitate radius (<r>), nm	Precipitate number density (N <sub>v</sub> ), m <sup>-3</sup>	Precipitate volume fraction (v <sub>f</sub> ), %
Al-3.1Ni-0.15Zr, annealed at 400 °C for 10 h	2.5 ± 1.0	1.30 × 10 <sup>22</sup>	0.20 ± 0.02
Al-3.1Ni-0.15Zr, annealed at 400 °C for 100 h	4.0 ± 1.0	5.10 × 10 <sup>21</sup>	0.18 ± 0.02

2.5 nm, the strengthening contributions from “ordering” and “coherency + modulus” were calculated to be of similar value and hence we took a contribution from the precipitates,  $\sigma_{precipitate}$ , to be 94 MPa. Similarly, for 100 h annealed sample having Al<sub>3</sub>Zr average precipitate size of 4.0 nm, strength contribution from Orowan looping ( $\sigma_{precipitate}$  ~88 MPa) is adopted.

#### 4.4. Total strength contribution from eutectic and precipitates in annealed Al-3.1Ni-0.15Zr alloy

Here, we assume that the strengthening mechanisms due to Al-Al<sub>3</sub>Ni eutectic and Al<sub>3</sub>Zr precipitates are operating independently and hence the total contribution can be taken as a sum of the individual contributions. To a reasonable first approximation, this assumption can be justified since the strengthening by the Al<sub>3</sub>Zr precipitates originates from coherency strains that obstruct the passage of dislocations. While the eutectic strengthening by the Al<sub>3</sub>Ni rods is primarily due to its modulus mismatch with the  $\alpha$ -Al matrix. Hence, the total yield strength of annealed Al-3.1Ni-0.15Zr alloy at room temperature can be estimated by the equation [53].

$$\sigma_{total} = \sigma_{eutectic} + \sigma_{precipitate} \quad (4)$$

For 10 h annealed alloy, The  $\sigma_{total}$  is estimated to be ~277 MPa while for 100 h annealed alloy it is ~256 MPa. The estimated total strength for the annealed Al-3.1Ni-0.15Zr alloys with their individual strengthening contributions was compared in Fig. 7(b) and also summarized in Table 3. From these results, we note that under identical annealing conditions at 400 °C for 100 h, the contribution to the strengthening from eutectic is significantly affected for Al-3.1Ni alloy compared to the same contribution for Al-3.1Ni-0.15Zr alloy. This might be due to enhanced resistance of eutectic microstructure against coarsening due to Zr addition in the alloy.

#### 4.5. Influence of Zr addition on eutectic coarsening kinetics

As mentioned in section 3.2, the eutectic rod spacing increases at a higher rate for Al-3.1Ni alloy during annealing at 400 °C compared to the Zr containing Al-3.1Ni-0.15Zr alloy, Fig. 2(f). Coarsening kinetics were determined from stereological measurements by equations discussed in section 2.4, and plotting the temporal evolution of average equivalent radius ( $R_{eq}$ ) of eutectic rods vs isothermal annealing time for both Al-3.1Ni and Al-3.1Ni-0.15Zr alloys at 400 °C (Fig. 8(a) and Table 5). The average  $R_{eq}$  increases continuously with annealing time for both the alloys.

However, the average  $R_{eq}$  for Al-3.1Ni-0.15Zr alloy at each time is lower than the Al-3.1Ni alloy. Further analysis can be done by using the coarsening equation [54–57].

$$\langle R_{eq}(t) \rangle^n = K_r t \quad (5)$$

where  $\langle R_{eq}(t) \rangle$  is the average equivalent radius at time  $t$ ,  $1/n$  is the temporal exponent and  $K_r$  is the eutectic rod coarsening rate constant. In equation (5),  $\langle R_{eq}(t) \rangle^n$  is preferred over directly using  $\langle R_{eq}(t) \rangle^3$  because it is free of the assumptions of the LSW-based model for dilute alloys. Fig. 8(b) shows the plot between  $\log[\langle R_{eq}(t) \rangle]$  vs  $\log(t)$  for both the alloys. The linear regression analysis for the data points gives the temporal exponent values of  $0.31 \pm 0.02$  for Al-3.1Ni and  $0.29 \pm 0.02$  for Al-3.1Ni-0.15Zr alloys. These values are close to 0.33 value predicted for LSW model that suggests diffusion controlled coarsening of Al<sub>3</sub>Ni eutectic rods in  $\alpha$ -Al matrix for both the alloys.

Smart et al. had also reported that the initial stage of Al<sub>3</sub>Ni rods coarsening in  $\alpha$ -Al follows the conventional LSW based coarsening model [26]. Fig. 8(c) shows the plot between  $\langle R_{eq}(t) \rangle^3$  vs annealing time for both the alloys. The linear regression analysis of the data points yields a coarsening rate constant values ( $K_r$ ) of 10.3 nm<sup>3</sup>/s for Al-3.1Ni and 4.1 nm<sup>3</sup>/s for Al-3.1Ni-0.15Zr alloys at 400 °C. Clearly, Zr addition to the binary Al-3.1Ni alloy has reduced the  $K_r$  value for the Al<sub>3</sub>Ni rods. In the binary Al-Ni alloys, high diffusivity of Ni in  $\alpha$ -Al results in two kind s of instabilities of Al<sub>3</sub>Ni rods at high temperatures: 1) eutectic morphological instability or spheroidization of Al<sub>3</sub>Ni rods and 2) eutectic size instabilities. The formation of faults during the solidification process has been reported to be the major cause for these instabilities that lead to the coarsening of the length scale of microstructure [23–25]. The increased microstructural stability for Al-3.1Ni-0.15Zr alloy in our study correlates with the absence of breaking/spheroidization of Al<sub>3</sub>Ni rods, unlike that observed in the binary Al-3.1Ni alloy [58]. The retention of a finer eutectic microstructure of Al-3.1Ni-0.15Zr alloy after 100 h of annealing at 400 °C results in higher strength compared to coarser Al-3.1Ni alloy. As shown in Table 3, the contribution of the eutectic to the overall strength is much larger and any change to this affects the strength properties. In the next section, we will show that this reduced coarsening rate is associated with the local distribution or enrichment of Zr solute at  $\alpha$ -Al/Al<sub>3</sub>Ni interface.

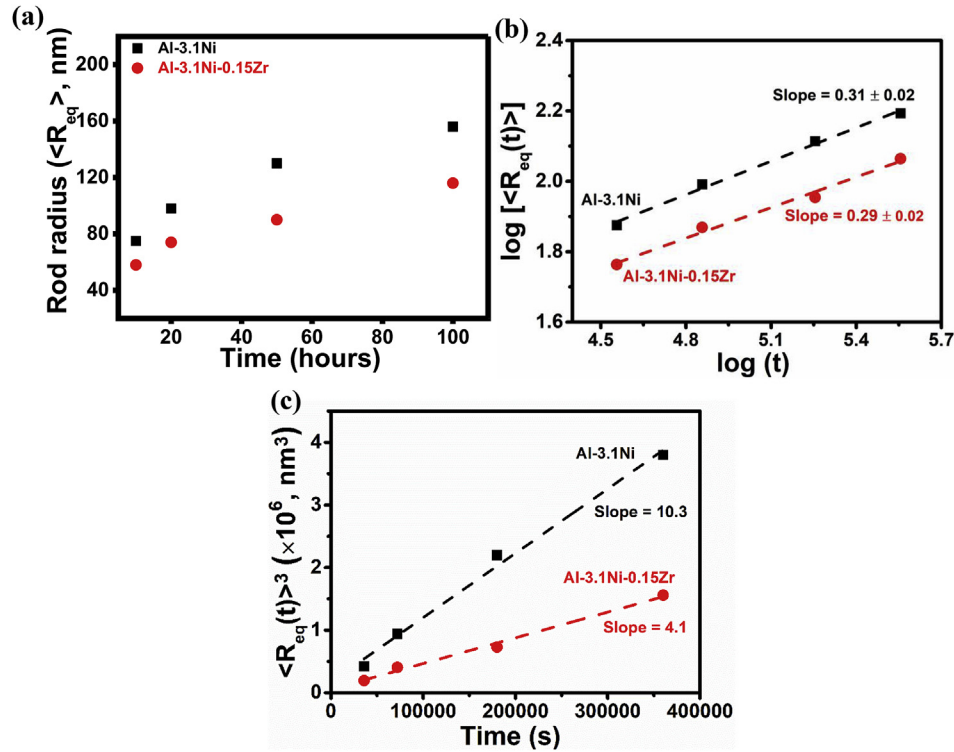


**Fig. 8.** (a) Temporal evolution of average equivalent rod radius ( $\langle R_{eq} \rangle$ ) for the Al-3.1Ni and Al-3.1Ni-0.15Zr alloys subjected to isothermal annealing at 400 °C. (b)  $\log(\langle R_{eq}(t) \rangle)$  vs  $\log(t)$  plots for both Al-3.1Ni and Al-3.1Ni-0.15Zr alloys give temporal exponent ( $1/n$ ) values that are close to the LSW model based predicted value. (c) The plots between  $\langle R_{eq}(t) \rangle^3$  and time ( $t$ ) on linear regression give LSW model based predicted coarsening rate constant values for Al-3.1Ni and Al-3.1Ni-0.15Zr alloys at 400 °C.

**Table 5**

Temporal evolution of the average equivalent rod radius ( $\langle R_{eq} \rangle$ ) for the Al-3.1Ni and Al-3.1Ni-0.15Zr alloys during isothermal annealing at 400 °C.

Heat treatment time (h)	Average equivalent rod radius ( $\langle R_{eq} \rangle \pm \sigma_R$ , nm)	
	Al-3.1Ni	Al-3.1Ni-0.15Zr
10	75.0 $\pm$ 0.8	58.0 $\pm$ 0.6
20	98.0 $\pm$ 1.0	74.0 $\pm$ 0.8
50	130.0 $\pm$ 1.1	90.0 $\pm$ 1.0
100	156.0 $\pm$ 1.6	115.0 $\pm$ 1.3

#### 4.6. The local distribution of Zr solute at $\alpha$ -Al/ $\text{Al}_3\text{Ni}$ interface and its influence on coarsening

The origin of coarsening resistance of  $\text{Al}_3\text{Ni}$  rods at 400 °C is due to distinct segregation of Zr solute at the  $\text{Al}_3\text{Ni}/\alpha\text{Al}$  interface (see Fig. 5(e)), while there is negligible segregation of Zr solute at the  $\text{Al}_3\text{Zr}/\text{matrix}$  interface. The diffusional motion of an interface in a solid can be expressed as [59,60].

$$v = \frac{ds}{dt} = M \times \gamma_{interface} / L \quad (6)$$

where  $v$  is the velocity of the interface,  $s$  is the displacement,  $M$  is a mobility term,  $\gamma_{interface}$  is the interface energy term and  $1/L$  is a measure of interface area per unit volume. In the case of a grain boundary, it represents the grain size, while for a spherical precipitate it will represent the precipitate size. We now consider the effect of Zr segregation at  $\alpha$ -Al/ $\text{Al}_3\text{Ni}$  rod interface on these terms.

As reported in the earlier literature, the interfacial segregation of the slow diffusing Zr atoms at the  $\alpha$ -Al/ $\text{Al}_3(\text{Sc}_{1-x}\text{Zr}_x)$  interface ( $D_{Zr \text{ in Al}} \text{ at } 400^\circ\text{C} = 1.2 \times 10^{-20} \text{m}^2/\text{s}$  and  $D_{Sc \text{ in Al}} \text{ at } 400^\circ\text{C} = 1.98 \times$

$10^{-17} \text{m}^2/\text{s}$ ) hinders the diffusion of the rate controlling Sc atoms through the matrix and, thereby, reduces the coarsening rate and stabilizes the precipitate morphology [29,61–63]. Similarly, slow diffusing V ( $D_{V \text{ in Al}} \text{ at } 400^\circ\text{C} = 4.85 \times 10^{-24} \text{m}^2/\text{s}$ ) is also shown to affect the coarsening kinetics and the creep properties by segregating at the  $\alpha$ -Al matrix and  $\text{Al}_3\text{Sc}/\text{Al}_3(\text{Sc,Zr})/\text{Al}_3(\text{Er,Sc,Zr,V})$  precipitates interface [64–66]. In the present case, the heat-treatment leads to a significant amount of Zr segregation (up to ~0.34 at.%) at the  $\alpha$ -Al/ $\text{Al}_3\text{Ni}$  interface (Fig. 5(e)). Thus, this is expected to decrease the mobility and restrict the transport of Ni solute through the aluminium matrix and hence reduce the coarsening rate of  $\text{Al}_3\text{Ni}$  rods. Additionally, Ozbien and Flower [67] have determined the vacancy binding energy of Zr in aluminum alloys to be ~0.24 eV. This high binding energy of Zr will trap effectively a large number of vacancies at the interface and will also contribute to slowing down of the solute transport across the  $\alpha$ -Al/ $\text{Al}_3\text{Ni}$  rod interface.

Another important aspect is the effect of Zr segregation on interfacial energy. The interfacial segregation of solutes at the  $\alpha$ -Al/precipitate interfaces has been recently evaluated through both experiments and computations [68]. The alloying and segregation of Au, Ag and Sn at the  $\alpha$ -Al/ $\theta'$  precipitate interface in Al-Cu alloys has been studied experimentally that reveals a reduction in the interfacial energy and thus significantly influences the microstructure and kinetics of the precipitation process [69–71]. Similarly, the effect of Sc addition on  $\alpha$ -Al/ $\theta'$  precipitate interface in Al-Cu alloys and their subsequent effect on thermomechanical properties has been studied recently [72]. Mg segregation at the  $\alpha$ -Al/ $\text{Al}_3\text{Sc}$  hetero-phase interface also lowers the interfacial energy [73]. An extensive theoretical investigation on segregation behavior of solutes has recently been performed for  $\alpha$ -Al/ $\theta'$  interface in terms of segregation energies of different solute atoms [68]. These authors have established a hierarchy of solutes to stabilize the precipitate matrix interface. The effect of solutes on eutectic microstructure in

a solid state is less well studied. In an earlier study on Cr–Cr<sub>3</sub>Si eutectic, it is shown that coarsening of the Cr<sub>3</sub>Si in the eutectic is interfacial controlled [74]. The addition of Re and Ce had led to their segregation at the interface that can lower the interface energy and significantly reduces the coarsening rate. Recently, an addition of Sc is shown to have an effect on retaining strength at high temperature in the Al–Al<sub>3</sub>Ni eutectic [12,39].

In the present investigation, we could obtain a clear evidence of Zr segregation at the eutectic  $\alpha$ -Al/Al<sub>3</sub>Ni interface through APT measurements. The interfacial segregation of a solute species  $i$  can be quantified by Gibbsian interfacial excess at an interface and that can be given as [75].

$$\Gamma_i = \frac{N_i^{int} - N_i^0}{A_{int}} \quad (7)$$

where  $N_i^{int}$  and  $N_i^0$  are the number of atoms  $i$  at the interface and the number of atoms  $i$  in the matrix per unit area,  $A_{int}$ . Based on the two data sets, the calculated Gibbsian interface excess for solute Zr is estimated in the range between +0.54 and +1.07 atoms/nm<sup>2</sup>. Hence, we expect and propose that this segregation behavior of Zr at the  $\alpha$ -Al/Al<sub>3</sub>Ni interface may lead to a reduction in interfacial energy, and thereby provides microstructural stability to Al–Ni–Zr ternary alloy in comparison to its Al–Ni binary alloy at high temperatures. However, the quantitative estimation of the interfacial energy provided by Zr segregation would require further study by detailed simulations which are beyond the scope of the present work.

#### 4.7. On the origin of enhanced high temperature strength of the ternary alloy

The observed tensile strength of Al–3.1Ni and Al–3.1Ni–0.15Zr alloys at 250 °C is shown in section 3.3 and Table 2. As mentioned, there is a significant drop in strength for the binary alloys at 250 °C. The UTS drops from 308 MPa at 25 °C to 132 MPa at 250 °C for Al–3.1Ni alloy. In contrast, the UTS of the annealed Al–3.1Ni–0.15Zr alloy (exposed at 400 °C for 10 h) at 250 °C is 218 MPa compared to a value of 350 MPa at room temperature. This significant difference can be related to the higher coarsening rate of eutectic for Al–3.1Ni alloy at 250 °C compared to Al–3.1Ni–0.15Zr alloy. This plays a major role in enhancing the strength of the ternary alloy at high temperature. At 250 °C, the Ni diffusivity in Al is calculated to be  $\sim 1.15 \times 10^{-18} \text{ m}^2/\text{s}$  [29] and hence the presence of very slow diffusing Zr solute ( $\sim 4.92 \times 10^{-26} \text{ m}^2/\text{s}$ ) at the  $\alpha$ -Al/Al<sub>3</sub>Ni interface results in hindering the diffusion of Ni atoms and hence resist the coarsening of the eutectic.

## 5. Conclusions

The present work on the influence of Zr addition to the binary Al–3.1Ni alloy can be summarized by the following points:

1. The Zr addition of 0.15 at.% to the Al–3.1Ni alloy shifts the eutectic composition to hypoeutectic with the inclusion of primary  $\alpha$ -Al phase at the eutectic colony boundaries.
2. Annealing of ternary Al–3.1Ni–0.15Zr alloy at 400 °C leads to an increase in the Vickers hardness values with peak values achieved after 10 h and remains stable thereafter. Whereas, the binary Al–3.1Ni alloy shows a continuous drop in the hardness value accompanied by spheroidization of Al<sub>3</sub>Ni rods and a rapid increase in the rod spacing as compared to the ternary Al–3.1Ni–0.15Zr alloy.

3. The 10 h annealed ternary Al–3.1Ni–0.15 alloy shows strength of  $350 \pm 11$  MPa compared to a value of  $308 \pm 14$  MPa for the binary Al–3.1Ni alloy.
4. The experimentally calculated exponent of the temporal evolution of average rod size during isothermal annealing at 400 °C was close to 0.33 for both alloys, suggesting coarsening process follows a classical matrix diffusion limited LSW based coarsening model. However, the coarsening rate of Al<sub>3</sub>Ni rods in Al–3.1Ni–0.15 alloy was less than half of that observed in Al–3.1Ni alloy.
5. The APT results present clear evidence of Zr segregation at the eutectic Al<sub>3</sub>Ni rod/ $\alpha$ -Al interface in the ternary alloy. The confinement of Zr atoms at the  $\alpha$ -Al/Al<sub>3</sub>Ni interface reduces the interfacial energy as well as mobility and hence reduces significantly the coarsening of the eutectic length scale of the Al–3.1Ni–0.15Zr alloy as compared to Al–3.1Ni alloy.
6. The synergistic effect of Al<sub>3</sub>Zr strengthened  $\alpha$ -Al phase and coarsening resistant Al–Al<sub>3</sub>Ni eutectic due to interfacial Zr segregation leads to an excellent high-temperature strength of 218 MPa at 250 °C for ternary Al–3.1Ni–0.15Zr alloy.

## Acknowledgments

The authors would like to acknowledge the microscopy and atom probe tomography facility available at the Advanced Facility for Microscopy and Microanalysis (AFMM) center, Indian Institute of Science, Bangalore and at the Max-Planck-Institut für Eisenforschung, Germany. KC is grateful for the financial support from Department of Science and Technology. The authors are grateful to U. Tezins and A. Sturm for their technical support of the atom probe tomography and focused ion beam facilities at the Max-Planck-Institut für Eisenforschung. SKM acknowledges financial support from the Alexander von Humboldt Foundation.

## Appendix A. Supplementary data

Supplementary data to this article can be found online at <https://doi.org/10.1016/j.actamat.2019.03.025>.

## Appendix A

The first strengthening contribution accounts for the change in chemical (bonding environment) order due to shearing of the precipitates. The shearing of the ordered precipitates from the mobile matrix dislocations comes at the cost of energy penalty owing to the formation energetically unfavorable anti-phase boundary (APB). Hence, the energy required to create this planar defect (APB) results in an increase in yield strength.

The increase in the strength due to order can be calculated by the following equation [48].

$$\Delta\sigma_{order} = \frac{0.81M\gamma_{APB}^{Al_3Zr}}{2b} \left( \frac{3\pi v_f}{8} \right)^{0.5} \quad (A1)$$

where,  $M = 3.06$  is the Taylor factor for the face centered cubic (fcc) Al matrix, which relates the strengthening stress of polycrystalline Al to the single crystal [76],  $\gamma_{APB}^{Al_3Zr} = 0.445 \text{ Jm}^{-2}$  is the anti-phase boundary (APB) energy of Al<sub>3</sub>Zr precipitate for the {111} plane [52],  $b$  is the magnitude of the Burgers vector (for Al  $\sim 0.286 \text{ nm}$ ) [77] and  $v_f$  is the precipitate volume fraction.

A second strengthening contribution originates due to the interaction between the dislocations and elastically strained matrix due to higher precipitates/matrix lattice mismatch ' $\delta$ ' (for Al–Sc,  $\delta = 1.32\%$  while for Al–Zr,  $\delta = 0.75\%$  [29]). The strengthening contribution from the misfit stress can be calculated by the

equation given below [48].

$$\Delta\sigma_{coherency} = M\chi(\varepsilon G_{Al})^{\frac{3}{2}} \left( \frac{2\langle r \rangle \nu_f}{G_{Al} b} \right)^{0.5} \quad (A2)$$

where,  $G_{Al}$  is the shear modulus of the  $\alpha$ -Al matrix (25.4 GPa at 25 °C) [77],  $\chi$  is a constant which has a value of 2.6 [48],  $\langle r \rangle$  is the average precipitate radius and  $\varepsilon$  is given by the following equation

$$\varepsilon = \left| \delta \left[ 1 + \frac{2G_{Al}(1 - 2\nu_{Al_3Zr})}{G_{Al_3Zr}(1 + \nu_{Al_3Zr})} \right] \right| \quad (A3)$$

where,  $G_{Al_3Zr}$  is the shear modulus of the  $Al_3Zr$  precipitate (57 GPa 25 °C) [78],  $\delta$  is the lattice mismatch between  $Al_3Zr$  precipitate and  $\alpha$ -Al matrix at 25 °C (+0.75%) [29], which is given by the equation

$$\delta = \frac{2(a_{Al_3Zr} - a_{Al})}{(a_{Al_3Zr} + a_{Al})} \quad (A4)$$

where,  $a_{Al_3Zr}$  and  $a_{Al}$  are the lattice parameters of  $Al_3Zr$  precipitate and  $\alpha$ -Al matrix, respectively. The third strengthening contribution to the yield strength for a shearable precipitate is due to the difference in the shear modulus between the  $L1_2$  ordered precipitate and the fcc Al matrix. The contribution of the modulus mismatch to the total strength is given by the following equation [48].

$$\Delta\sigma_{modulus} = 0.0055 Mb (\Delta G)^{\frac{3}{2}} \left( \frac{2\nu_f}{G_{Al} b^2} \right)^{0.5} \left( \frac{\langle r \rangle}{b} \right)^{\left( \frac{3m}{2} - 1 \right)} \quad (A5)$$

where,  $\Delta G$  is the difference in the shear moduli between the  $Al_3Zr$  precipitate and  $\alpha$ -Al matrix (31.6 GPa) and  $m=0.85$  is a constant [48].

An alternate strengthening mechanism, the Orowan mechanism, operates when the size is larger. This involves looping of the advancing mobile dislocations around the precipitates and bypassing the obstacles, thus increasing the strength. The stress ( $\Delta\sigma_{Orowan}$ ) required for the dislocation to bypass the  $L1_2$  ordered spherical precipitates can be estimated by the formula [48,79–81].

$$\Delta\sigma_{Orowan} = \left( \frac{0.4MG_{Al}b}{\pi\sqrt{1-\nu}} \right) \left( \frac{1}{\lambda} \right) \left( \ln \frac{\pi\langle r \rangle}{2b} \right) \quad (A6)$$

where,  $\nu$  is the Poisson's ratio (0.345) [76] and  $\lambda$  is the average planar inter-precipitate distance.

The average inter-precipitate distance for the spherical precipitates can be estimated as [48,82].

$$\lambda = \langle r \rangle \left( \sqrt{\frac{2\pi}{3\nu_f}} - \frac{\pi}{2} \right) \quad (A7)$$

For the shearable precipitates, the coherency and modulus strengthening ( $\Delta\sigma_{coherency} + \Delta\sigma_{modulus}$ ) and the order strengthening ( $\Delta\sigma_{order}$ ) contribute to strength. Generally, for the strong chemically ordered precipitates the latter factor dominates while for others, the former dominates [33,49,51].

## References

- [1] W.S. Miller, L. Zhuang, J. Bottema, A.J. Wittebrood, P. De Smet, A. Haszler, A. Viergege, Recent development in aluminium alloys for the automotive industry, *Mater. Sci. Eng., A* 280 (2000) 37–49, [https://doi.org/10.1016/S0921-5093\(99\)00653-X](https://doi.org/10.1016/S0921-5093(99)00653-X).
- [2] J.A. Lee, *Cast aluminum alloy for high temperature applications*, vol. 8, 2003.
- [3] W. Reif, J. Dutkiewicz, R. Ciach, S. Yu, J. Król, Effect of ageing on the evolution of precipitates in AlSiCuMg alloys, *Mater. Sci. Eng., A* 234–236 (1997) 165–168, [https://doi.org/10.1016/S0921-5093\(97\)00181-0](https://doi.org/10.1016/S0921-5093(97)00181-0).
- [4] R. Kilaas, V. Radmilovic, Structure determination and structure refinement of  $Al_2CuMg$  precipitates by quantitative high-resolution electron microscopy, *Ultramicroscopy* 88 (2001) 63–72, [https://doi.org/10.1016/S0304-3991\(00\)00107-8](https://doi.org/10.1016/S0304-3991(00)00107-8).
- [5] D.G. Eskin, Decomposition of supersaturated solid solutions in Al–Cu–Mg–Si alloys, *J. Mater. Sci.* 38 (2003) 279–290, <https://doi.org/10.1023/A:1021109514892>.
- [6] Z. Ma, E. Samuel, A.M.A. Mohamed, A.M. Samuel, F.H. Samuel, H.W. Doty, Parameters controlling the microstructure of Al–11Si–2.5Cu–Mg alloys, *Mater. Des.* 31 (2010) 902–912, <https://doi.org/10.1016/j.matdes.2009.07.033>.
- [7] F.J. Tavitas-Medrano, A.M.A. Mohamed, J.E. Gruzleski, F.H. Samuel, H.W. Doty, Precipitation-hardening in cast Al–Si–Cu–Mg alloys, *J. Mater. Sci.* 45 (2009) 641, <https://doi.org/10.1007/s10853-009-3978-6>.
- [8] R. Martinez, V. Russier, J.P. Couzinié, I. Guillot, G. Cailletaud, Modeling of the influence of coarsening on viscoplastic behavior of a 319 foundry aluminum alloy, *Mater. Sci. Eng., A* 559 (2013) 40–48, <https://doi.org/10.1016/j.msea.2012.07.096>.
- [9] A. Poznak, R.K.W. Marceau, P.G. Sanders, Composition dependent thermal stability and evolution of solute clusters in Al–Mg–Si analyzed using atom probe tomography, *Mater. Sci. Eng., A* 721 (2018) 47–60, <https://doi.org/10.1016/j.msea.2018.02.074>.
- [10] B. Cantor, G.A. Chadwick, The growth crystallography of unidirectionally solidified Al–Al3Ni and Al–Al2Cu eutectics, *J. Cryst. Growth* 23 (1974) 12–20, [https://doi.org/10.1016/0022-0248\(74\)90035-9](https://doi.org/10.1016/0022-0248(74)90035-9).
- [11] B. Cantor, G.A. Chadwick, Crystallography of Al–Al3Ni, Al–Al2Cu and Al–Zr (AlAg) eutectics during nucleation and the early stages of growth, *J. Cryst. Growth* 30 (1975) 101–108, [https://doi.org/10.1016/0022-0248\(75\)90207-9](https://doi.org/10.1016/0022-0248(75)90207-9).
- [12] C. Suwanprecha, P. Pandey, U. Patakham, C. Limmaneevichitr, New generation of eutectic Al–Ni casting alloys for elevated temperature services, *Mater. Sci. Eng., A* 709 (2018) 46–54, <https://doi.org/10.1016/j.msea.2017.10.034>.
- [13] C.S. Tiwary, S. Kashyap, D.H. Kim, K. Chattopadhyay, Al based ultra-fine eutectic with high room temperature plasticity and elevated temperature strength, *Mater. Sci. Eng., A* 639 (2015) 359–369, <https://doi.org/10.1016/j.msea.2015.05.024>.
- [14] C. Suwanprecha, J.P. Toinin, R.A. Michi, P. Pandey, D.C. Dunand, C. Limmaneevichitr, Strengthening mechanisms in AlNiSc alloys containing Al3Ni microfibers and Al3Sc nanoprecipitates, *Acta Mater.* 164 (2019) 334–346, <https://doi.org/10.1016/j.actamat.2018.10.059>.
- [15] T. Koutsoukis, M.M. Makhlof, Alternatives to the Al–Si eutectic system in aluminum casting alloys, in: *Inter Metalcast*, vol. 10, 2016, pp. 342–347, <https://doi.org/10.1007/s40962-016-0042-6>.
- [16] Y. Fan, M.M. Makhlof, The effect of introducing the Al–Ni eutectic composition into Al–Zr–V alloys on microstructure and tensile properties, *Mater. Sci. Eng., A* 654 (2016) 228–235, <https://doi.org/10.1016/j.msea.2015.12.044>.
- [17] H. Okamoto, Al–Ni (aluminum–nickel), *JPE* 14 (1993) 257–259, <https://doi.org/10.1007/BF02667823>.
- [18] J.L. Murray, A.J. McAlister, The Al–Si (Aluminum–Silicon) system, in: *Bulletin of Alloy Phase Diagrams*, vol. 5, 1984, p. 74, <https://doi.org/10.1007/BF02868729>.
- [19] N.A. Belov, A.N. Alabin, D.G. Eskin, Improving the properties of cold-rolled Al–6%Ni sheets by alloying and heat treatment, *Scripta Mater.* 50 (2004) 89–94, <https://doi.org/10.1016/j.scriptamat.2003.09.033>.
- [20] Y.G. Nakagawa, G.C. Weatherly, The thermal stability of the rod Al3Ni–Al eutectic, *Acta Metall.* 20 (1972) 345–350, [https://doi.org/10.1016/0001-6160\(72\)90027-2](https://doi.org/10.1016/0001-6160(72)90027-2).
- [21] G.A. Chadwick, Eutectic alloy solidification, *Prog. Mater. Sci.* 12 (1963) 99–182, [https://doi.org/10.1016/0079-6425\(63\)90037-9](https://doi.org/10.1016/0079-6425(63)90037-9).
- [22] W.H.S. Lawson, H.W. Kerr, Mechanical behavior of rapidly solidified Al–Al2Cu and Al–Al3Ni composites, *Muzicki talas* 2 (1971) 2853–2859, <https://doi.org/10.1007/BF02813263>.
- [23] H.E. Cline, Shape instabilities of eutectic composites at elevated temperatures, *Acta Metall.* 19 (1971) 481–490, [https://doi.org/10.1016/0001-6160\(71\)90002-2](https://doi.org/10.1016/0001-6160(71)90002-2).
- [24] A.J. Ardell, Isotropic fiber coarsening in unidirectionally solidified eutectic alloys, *Muzicki talas* 3 (1972) 1395–1401, <https://doi.org/10.1007/BF02643023>.
- [25] H.B. Smartt, L.K. Tu, T.H. Courtney, Elevated temperature stability of the Al–Al3Ni eutectic composite, *Metall. Trans.* 2 (1971) 2717–2727, <https://doi.org/10.1007/BF02814917>.
- [26] H.B. Smartt, T.H. Courtney, The kinetics of coarsening in the Al–Al3Ni System, *MTA* 7 (1976) 123–126, <https://doi.org/10.1007/BF02644047>.
- [27] M.E. Fine, Precipitation hardening of aluminum alloys, *MTA* 6 (1975) 625–630, <https://doi.org/10.1007/BF02672283>.
- [28] R.W. Hyland, Homogeneous nucleation kinetics of Al3Sc in a dilute Al–Sc alloy, *MTA* 23 (1992) 1947–1955, <https://doi.org/10.1007/BF02647542>.
- [29] K.E. Knippling, D.C. Dunand, D.N. Seidman, Criteria for developing castable, creep-resistant aluminum-based alloys – a review, *MEKU* 97 (2006) 246–265, <https://doi.org/10.3139/146.101249>.
- [30] S.K. Makineni, S. Sugathan, S. Meher, R. Banerjee, S. Bhattacharya, S. Kumar, K. Chattopadhyay, Enhancing elevated temperature strength of copper containing aluminum alloys by forming L1 2 Al 3 Zr precipitates and nucleating  $\theta''$  precipitates on them, *Sci. Rep.* 7 (2017) 11154, <https://doi.org/10.1038/s41598-017-11540-2>.
- [31] S. Mondol, S.K. Makineni, S. Kumar, K. Chattopadhyay, Enhancement of high temperature strength of 2219 alloys through small additions of Nb and Zr and

